MOEM

Modern Electronic Materials 2021; 7(4): 127–139
DOI 10.3897/j.moem.7.4.78587

Research Article

Electrical and galvanomagnetic properties of black phosphorus single crystals

Andrei A. Kharchenko[1], Julia A. Fedotova[1], Valeryia Yu. Slabukho[2], Alexander K. Fedotov[1], Alexey V. Pashkevich[1,2], Ivan A. Svito[2], Maxim V. Bushinsky[3]

1 Research Institute for Nuclear Problems of Belarusian State University, 11 Bobruiskaya Str., Minsk 220006, Belarus

2 Belarusian State University, 4 Nezalezhnosti Ave., Minsk 220030, Belarus

3 SSPA "Scientific-Practical Materials Research Centre of NAS of Belarus", 19 P. Brovki Str., Minsk 220072, Belarus

Corresponding author: Alexander K. Fedotov (fedotov@bsu.by)

Received 28 November 2021 ♦ **Accepted** 17 December 2021 ♦ **Published** 30 December 2021

Citation: Kharchenko AA, Fedotova JuA, Slabukho VYu, Fedotov AK, Pashkevich AV, Svito IA, Bushinsky MV (2021) Electrical and galvanomagnetic properties of black phosphorus single crystals. *Modern Electronic Materials* 7(4): 127–139. https://doi.org/10.3897/j.moem.7.4.78587

Abstract

Black phosphorus (b-P) single crystals having the n-type electrical conductivity produced in a high pressure set-up (~1 GPa) with six diamond anvils at 800 °C for 12 h have been studied. The electrical conductivity $\sigma(T,B)$ and the Hall constant $R_h(T,B)$ have been analyzed within one-band and two-band models as functions of temperature in the $2 < T < 300$ K range and magnetic field in the $0 < B < 8$ T range. Fitting of the experimental $\sigma(T,B)$ and $R_h(T,B)$ curves suggests the following key properties of the crystals: (1) intrinsic conductivity type, (2) approximately equal electron and hole concentrations and mobilities, (3) anisotropic behavior of electron and hole conductivities, concentrations and mobilities and (4) combination of negative and positive contributions to magnetoresistance (magnetoresistive effect, MR). In a zero magnetic field the anisotropy coefficient $\alpha = [\sigma_a(T) - \sigma_c(T)]/\sigma_c(T)$ below 50–70 K is positive whereas above 220 K its sign changes to negative due to a specific combination of the temperature dependences of carrier concentration and mobility. It has been shown that the negative sign of relative MR (negative magnetoresistive effect) dominates at $T < 25$ K and $B < 6$ T and is presumably caused by the effects of strong localization resulting from structural disorder. The positive MR sign (positive magnetoresistive effect) is associated with the Lorentz mechanism of carrier movement and exhibits itself above 25 K in 6–8 T magnetic fields.

Keywords

black phosphorus, conductivity anisotropy, magnetoresistance, carrier transport, two-band model.

1. Introduction

Black phosphorus **(b-P)** is one of the most atmospheric-pressure stable allotropic phosphorus modifications pertaining to the series of materials having a new-type layered 2D structure [1–3]. Figure 1 shows schematic view of the crystal lattice of b-P single crystals. It can be seen from Fig. 1 that its crystal lattice is orthorhombic (*Cmca*) with eight atoms per unit cell and has a rifled double layered structure with a system of parallel ridges and troughs [4–6]. The phosphorus atoms in the layers are bound with three closest neighbors by covalent bonds of unpaired electrons. It has been reported [7–9] that the angles between the bonds are $\theta_{213} = 96.34°$ and $\theta_{145} = 102.09°$, the bond lengths are $d_1 = 0.2224$ nm and $d_2 = 0.2244$ nm and the lattice parameters along the crystallographic axes are $a = 0.4376$ nm, $b = 1.0478$ nm and $c = 0.3314$ nm.

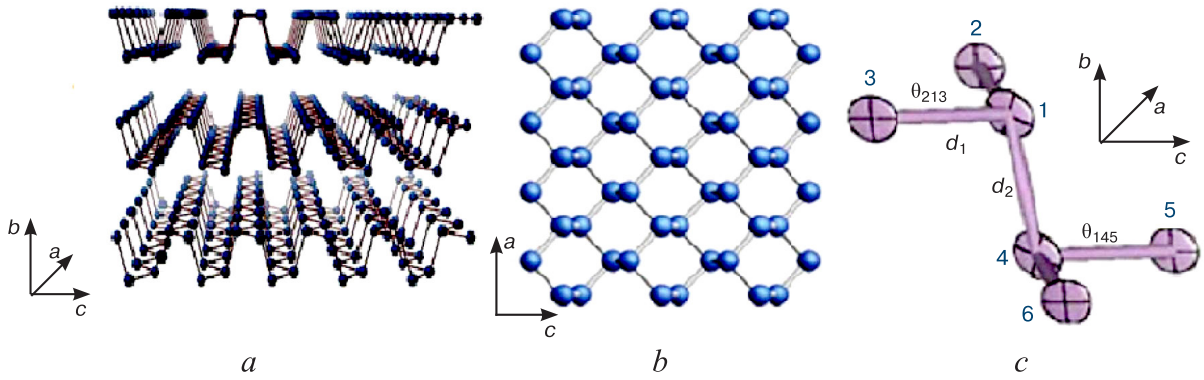

Figure 1. (*a*) Schematic of rifled layered structure, (*b*) layer top view and (*c*) layer fragment in b-P lattice [4, 5].

The layers are bound by Van der Waals forces, the interlayer distances being approximately 50% greater than the interatomic distances inside the layers which is evident from the lattice parameters presented above.

As can be seen from Fig. 1 *a*, because of the atomic positions in the black phosphorus crystal lattice there are two non-equivalent directions: the zigzag shaped one (ZZ, parallel to the atomic ridges) and the armchair-shaped one (AC, perpendicular to the ridges) [8, 10]. This anisotropy is typically described using three axes *a*, *b* and *c* where the *a* and *c* axes are parallel to the layers and perpendicular to each other and to the *b* axis, with the *b* axis being perpendicular to the layers.

Studies of bulk black phosphorus started after P.U. Bridgman first synthesized it in 1914 at high pressures and temperatures [11]. However in the 2000s when the layered structure of b-P and other specific features of its electrical conductivity (see below) were first used, an intense study of single- and multilayered graphene-like 2D structures and layered transition metal chalcogenides started (see references in monographs and overviews [1, 12–16]). Low-dimensional b-P (referred to as phosphorene) is of great interest thanks to its useful properties such as narrow and adjustable direct band gap (0 to 0.3 eV), high carrier mobility, strong anisotropy in the plane of the Van der Waals bound layers as well as a large specific surface area. Furthermore of practical interest are the attractive photothermal properties, biocompatibility, biodegradability and other properties of black phosphorus [17–19]. For this reason phosphorene researchers pay special attention to applications such as energy conversion and storage, oxygen extrication, electronics, optoelectronics, photocatalytic hydration, water splitting, thermoelectric generators etc.

Despite the obvious success in phosphorene research there are still a number of pending questions in the understanding and explanation of the properties (primarily, electric ones) of bulk b-P crystals. Below is a brief overview of literary data on the electrical properties of bulk polycrystalline and single crystalline black phosphorus obtained using various methods.

Works dealing with the properties of black phosphorus can be arbitrarily divided in 2 groups: in the period from 1914 to approx. 1990 [2, 6, 20–24] and after 2014 [1, 3–5, 7–19, 25–33] when interest to b-P arose again due to the production of b-P single crystals having a higher structural perfection. There are multiple literary data on the electrical resistivity and Hall effect of bulk b-P single crystals over a wide range of temperatures and magnetic fields [20–28] and at different pressures. These data show that the room temperature electrical resistivity ρ_{300} and the Hall mobility μ_{300} of bulk b-P specimens exhibit a large scatter, i.e., 0.02–60 Ohm and 30–4000 $cm^2/(V \cdot s)$, respectively. This wide scatter of these parameters is primarily caused by the difference in the structural perfection of tested crystals. Studies of $\rho(T)$ for bulk b-P specimens over a wide temperature range (2–725 K) [20–28, 33] showed a quite complex pattern of the temperature dependences of their electrical resistivity $\rho(T)$. It was also shown [20–28, 33] that with an increase in temperature $\rho(T)$ of b-P crystals initially decreases reaching a minimum at approx. 60–100 K, reaches a maximum at 250–500 K and then starts to decline again. Although this trend of resistivity as a function of temperature is quite complex and the temperature ranges in which the abovementioned minimum and maximum of $\rho(T)$ occur differ significantly, the data are in a good agreement in general.

As noted above, earlier data [20, 24, 25, 27, 29–33] suggest (see for example Fig. 3) that the layered structure of b-P single crystals is exhibited in the high anisotropy of carrier transport and largely affects the pattern of the Hall constant $R_h(T,B)$ as well as $\rho(T,B)$ and $\mu(T,B)$ as functions of temperature and magnetic field for electric current flow along three different axes (*a*, *b* and *c*) of the crystals. Earlier studies showed [2, 20, 23–26, 29–37] that the electrical conductivity and mobility are always the highest in the *ac* plane of the single crystals, and on the whole they decrease in the sequence $\sigma_c > \sigma_a > \sigma_b$ [2, 23, 24, 33].

As noted earlier [24] the scatter of the electrical resistivity and carrier mobility in the crystals can originate not only from differences in the quality of the crystals but also from the sampling and crystal axes orientation accuracy relative to the current flow direction. The effect of b-P crystal imperfections on the anisotropy of the

electrical properties of the crystals was studied in detail earlier [2, 24, 33]. It was shown [2, 24, 33] that the scatter of the specific electrical resistivity data along the *b* axis (perpendicular to the layers bound with Van der Waals bonds) and the discrepancy with the data on the effective carrier mass (especially at low temperatures) are due to the presence of stacking faults and other types of imperfections in the crystals along this axis. Furthermore there are indications [20, 30, 36] that the atomic structure anisotropy in black phosphorus leads to a strong anisotropy of the dispersion law and effective mass of carriers in the allowed band which further contributes to the orientation dependence of the carrier mobility and conductivity not only in single crystals but also in single- and multilayered b-P specimens.

The behavior of anisotropic semiconductors and semimetals (especially those having nontrivial carrier dispersion laws) in magnetic fields plays a key role in the understanding of their carrier transport mechanisms. The first data on the magnetoresistive effect in b-P crystals were reported in the earliest works on the topic [23, 24] in which the authors first noted the existence of two contributions to the relative magnetoresistance MR = $[\rho(B) - \rho(0)]/\rho(0)] \cdot 100\%$, i.e., positive magnetoresistance **(PMR)** at high temperatures ($T > 77$ K) and negative one **(NMR)** at lower temperatures ($T < 4$ K). Scarce studies after 2014 [20, 32–40] reported contradictory results on the behavior of the electrical resistivity of black phosphorus single crystals in magnetic fields. The most detailed study of MR reported so far [35] was carried out for the following experimental conditions: current flow is along the *c* axis and the **B** vector is perpendicular to the *ac* plane of the single crystal. It was reported [35] the lack of NMR and a giant PMR of 510% occurs at magnetic field with induction $B = 7$ T at $T = 30$ K. The test single crystal [35] exhibited a transition from the parabolic (Lorentz-like) to the linear $\rho(B)$ dependence. Due to the inhomogeneity of the test single crystals the PMR was attributed to the large-scale potential relief **(LSPR)** which caused carrier mobility fluctuations. The parabolic Lorentz contribution to the PMR which dominated at $B < B_L$ was confirmed by the adherence to Kohler's rule [37] which indicates the existence of a single scattering process in the n-P single crystal under study.

The PMR to NMR transition [38] was confirmed to occur as a result of black phosphorus single crystal cooling below 10 K in $B < 5$ T magnetic fields. At higher temperatures the PMR grew with an increase in temperature and after the maximum of approx. 100% at a $T = 40$ K PMR contribution declined with a further increase in temperature (by ~10% at 300 K). Furthermore it was reported [37] that the PMR values were always higher for field induction vector **B** orientation parallel to the *c* axis in comparison with that for **B** vector orientation parallel to the *b* axis. Two interesting features of the effect of magnetic field on carrier transport under electric field were reported [38, 39]:

1. With an increase in the magnetic field the longitudinal contribution to the resistivity tensor $\rho_{xx}(B)$ does not undergo saturation in the PMR region whereas in the NMR region its saturation occurs.

2. The Hall resistivity $\rho_{xx}(B)$ grows linearly with an increase in the magnetic field at 3 and 300 K but exhibits a nonlinear behavior in the entire range of intermediate temperatures, i.e., 20–200 K.

The former specific feature of the $\rho_{xx}(B)$ behavior under impact of magnetic field results in necessity to describe it by two models, i.e., the classical resistor array model (caused by disorder) and the magnetic polaron model (due to the high ohmicity of the crystal) [38, 39]. The former model dominates at higher temperatures and the latter one, in the low-temperature range.

The latter specific feature of the $\rho_{xx}(B)$ behavior in a magnetic field is accounted for on the basis of two-band conductivity models involving two types of carriers.

Analysis of literary data on carrier transport in bulk black phosphorus crystals discovers a wide range of

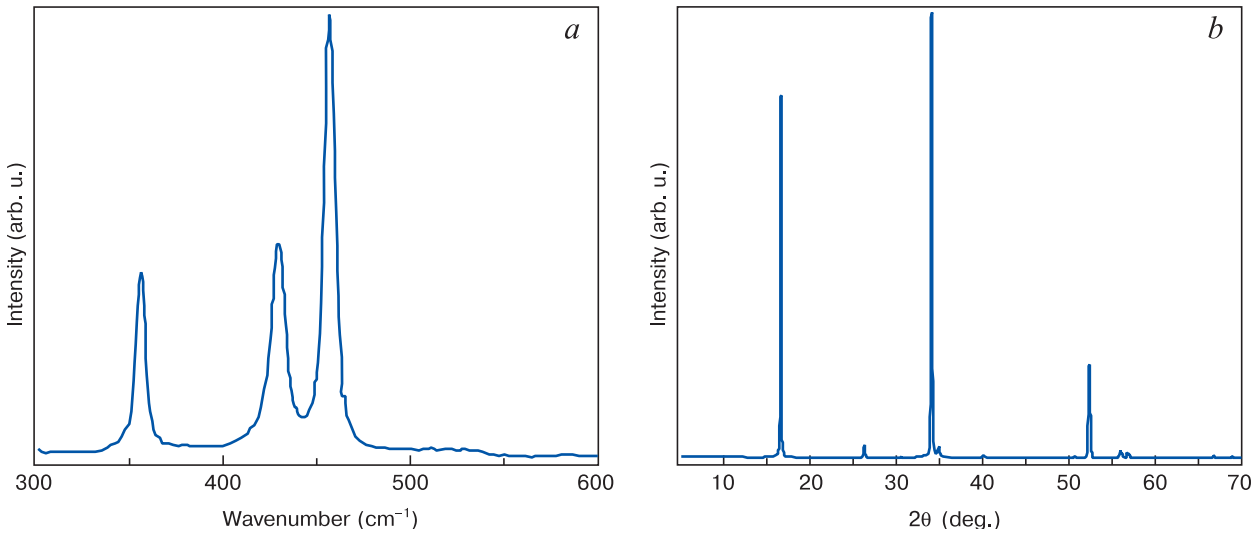

Figure 2. (*a*) Raman spectrum and (*b*) X-ray diffraction pattern of black phosphorus single crystal.

models based on which black phosphorus electrical properties are described. It should be noted that there are scarce data on the influence of b-P crystal growth technology (primarily, synthesis process pressure, temperature duration and atmosphere), defect state (single crystal, polycrystal, type and quantity of defects, deformation etc.) and measurement mode (number of heating/cooling cycles, storage time and atmosphere) on the temperature dependences of electrical resistivity, magnetoresistive effect, Hall effect, Seebeck effect and other properties of the material. For this reason a number of questions as to the nature of the electrical properties formation in black phosphorus bulk crystals have not been clarified as yet.

Below we present data on the temperature dependences of the electrical conductivity, magnetoresistance and Hall effect for several b-P bulk single crystals made by 2D Semiconductors, USA.

2. Experimental

The single crystals were synthesized in a high pressure plant (~1 Gpa) with six diamond anvils at 800 °C for 12 h following a technology similar to a earlier described one [41]. The structure of the crystals was certified by the manufacturer using X-ray diffraction and Raman spectroscopy (Fig. 3).

Standard measurements of the electrical resistivity $R(T,B)$ and the Hall constant $R_h(T,B)$ of the black phosphorus single crystals were carried out in the $2 < T < 300$ K temperature range at $0 \le B < 8$ T magnetic fields. The test specimens were rectangular, their longer sides (and hence the current vector directions) being parallel to the *a* crystallographic axis (Specimen 1) or the *c* axis (Specimen 2) and the **B** vector being always perpendicular to the *ac* plane, i.e., it was along the *b* axis. The $R(T,B)$ and $R_h(T,B)$ dependences were recorded in a cryogen-free measurement system of Cryogenics Ltd., UK, on the basis of a closed-cycle refrigerator. The current through the specimens during the measurements was set and measured with a Keithley 6430 unit which allows measuring electrical resistance in the 100 mΩ to 10 GΩ range accurate to within 0.1%. The temperature of the specimens was controlled with LakeShore thermodiodes calibrated accurate to 0.0005 K and having a reproducibility of 0.001 K. The temperature was stabilized and measured with a LakeShore 331 controller. The measurement accuracy of the conductivity σ and the Hall constant R_h was not worse than 5%, the error being mostly determined by the measurement error in specimen dimensions, electric contact width and contact spacing. Room temperature Hall effect and Seebeck effect sign measurements showed that the test single crystals had the *n* type conductivity. The stability of the Hall effect sign testified to the predominantly electron conductivity over the whole test temperature range. The quality of the contacts for all the specimens was checked by preliminary measurement of IVs at $T = 300$ K which proved to be linear at currents of below 1 mA.

3. Results and discussion

Figure 3 shows typical temperature dependences of the conductivity and the Hall constant for two crystals (Specimens 1 and 2) in which the current was oriented along the longer sides (the *a* and *c* axes appropriately) and the magnetic field was always perpendicular to the wider face, i.e., the *ac* plane.

The tests showed that the b-P specimens exhibit a strong conductivity anisotropy showing itself primarily in the difference between the behavior of $\sigma_a(T)$ and $\sigma_c(T)$ in the measuring temperature range with the current vector

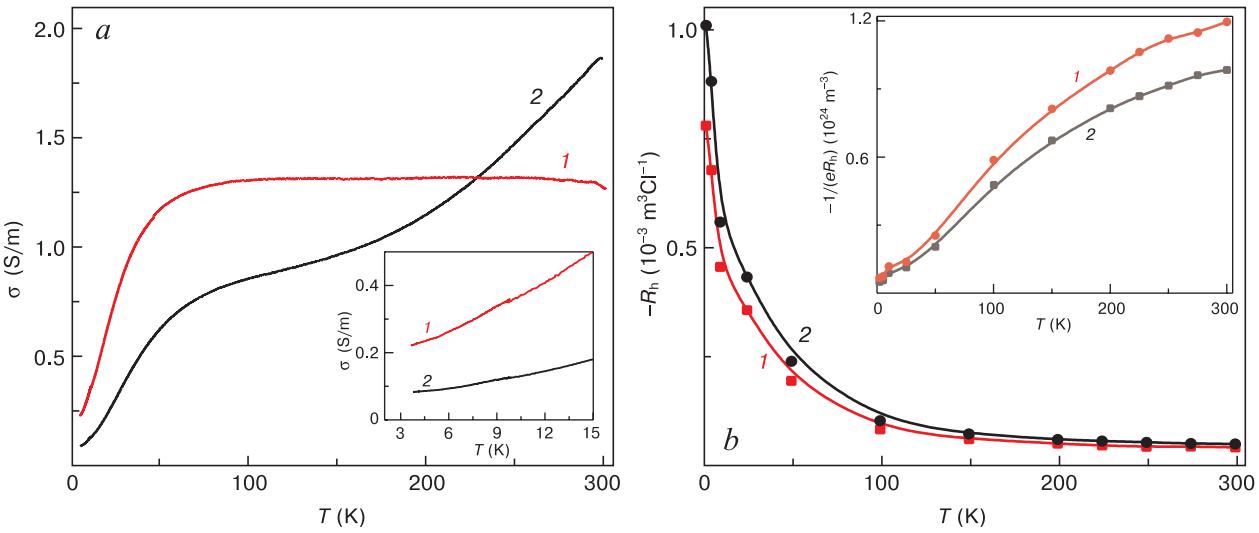

Figure 3. Temperature dependences of (*a*) conductivity σ and (*b*) Hall constant R_h in $B = 8$ T magnetic field for current flow along (*1*) the *a* axis and (*2*) the *c* axis of b-P bulk crystals. Insets: (*a*) σ(T) at $T \le 15$ K and (*b*) Hall carrier concentration for the single-band model.

being always oriented along the *a* or *c* axes, respectively. It can be seen from Fig. 3 *a* that for current flow along the *c* axis the $\sigma_c(T)$ curve course for Specimen 2 in the entire 2–300 K range (Curve *2*) is typical of semiconductors. In the meantime the $\sigma_a(T)$ curve course for Specimen 1 (i.e., for current flow along the *a* axis, Fig. 3 *a*, Curve *1*) above 50–70 K is almost the same as the $\sigma(T)$ curve of metals. In the semiconductor range it is always true that $\sigma_a(T) > \sigma_c(T)$, i.e., the presence of ridges in the b-P atomic structure produces additional barriers to carrier movement. Below 50–70 K the anisotropy coefficient $\alpha = [\sigma_a(T) - \sigma_c(T)]/\sigma_c(T)$ is positive whereas above 220 K its sign changes to negative, and therefore the $\sigma_a(T)$ curve in Fig. 3 *a* lies below $\sigma_c(T)$. An additional specific feature of the $\sigma_a(T)$ and $\sigma_c(T)$ curves is their saturation upon specimen cooling below 10 K (Fig. 3 *a*, inset).

The test showed that $R_h(B)$ in fields stronger than 1 T at any temperatures is almost insensitive to magnetic field magnitude. Figure 3 *b* shows Hall constant as a function of temperature $R_h(T)$ in the magnetic field of B = 8 T for Specimens 1 and 2. The close behavior of these dependences indicates a weak anisotropy: the $R_h(T)$ curve measured along the *a* axis proves to be on average by only 20% lower than the one measured along the *c* axis. Since for single type of carriers the carrier concentration is inversely proportional to the Hall constant, this $R_h(T)$ behavior at low temperatures correlates with the behavior of the $\sigma_a(T)$ and $\sigma_c(T)$ curves. Furthermore it can be seen from the inset in Fig. 3 *b* that the temperature dependence of the Hall electron concentration $1/eR_h(8\ \text{T})$ in Arrhenius' coordinates becomes linear above 70 K that allows to estimate the defect ionization energy E_i and the effective electron concentration n_o in the b-P single

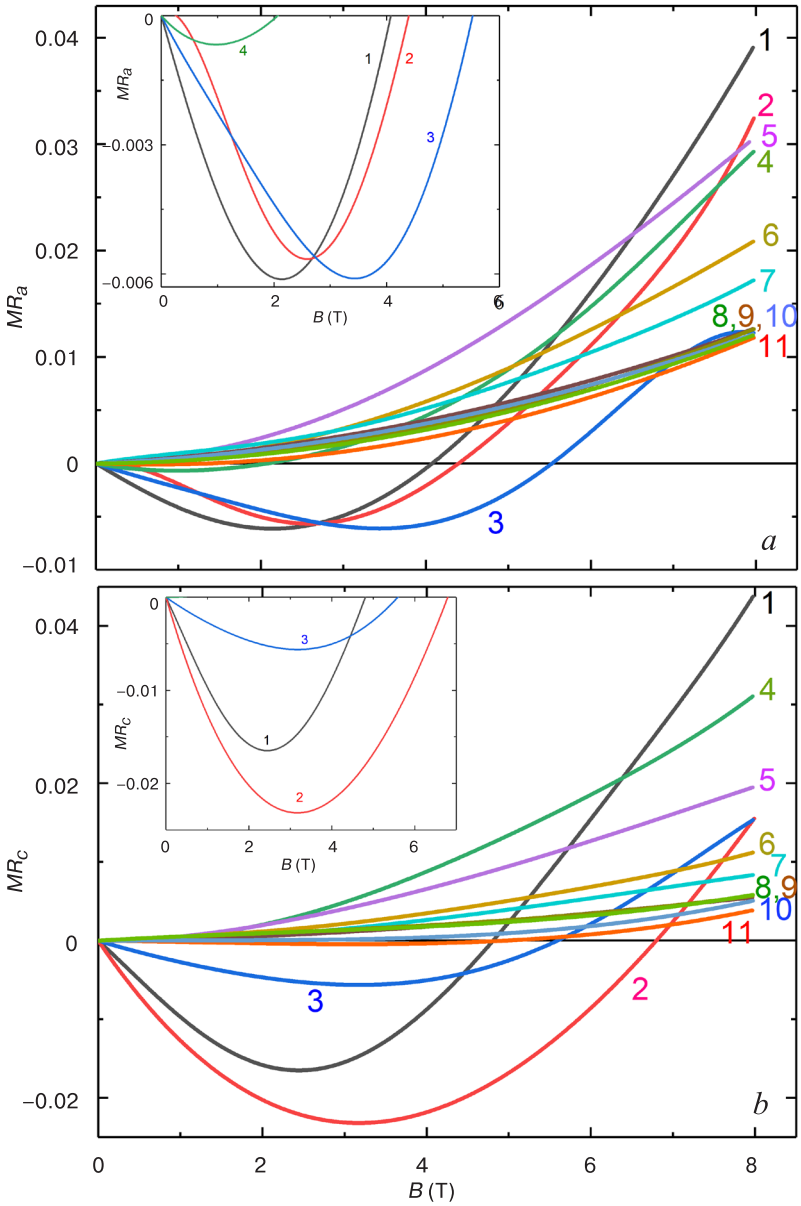

Figure 4. Relative magnetoresistance $MR(B,T)$ for black phosphorus specimens (*a*) 1 and (*b*) 2 as a function of magnetic field B at different temperatures T, K: (*1*) 2; (*2*) 5; (*3*) 10; (*4*) 25; (*5*) 50; (*6*) 100; (*7*) 150; (*8*) 200; (*9*) 250; (*10*) 275; (*11*) 300.

crystals within the single-band model [24, 41, 42]. These estimates suggest that E_i for Specimens 1 and 2 are 9.13 and 9.39 meV, respectively, and n_o are $2.12 \cdot 10^{-23}$ and $1.79 \cdot 10^{-23}$ m^{-3}, respectively. It should be noted that E_i for the test specimens are more than 3 times lower than the band gap $E_g \approx 0.31 \div 0.37$ eV according to earlier estimates [2, 22, 24, 41] for intrinsic b-P single crystals. The E_i estimates shown above prove to be close to earlier literary data which were also obtained within the single-band model but the electron concentrations are higher as compared with our [42] and others' [22, 39] estimates made on the basis of the two-band model (see below) which implies the existence of two different-sign carrier types in b-P crystals.

To correctly estimate the carrier concentrations and adequately describe the carrier transport mechanisms in single crystal b-P Specimens 1 and 2 we additionally studied the relative magnetoresistance $MR(B,T) = [R(B) - R(0)]/R(0)$ as a function of magnetic field and temperature (Fig. 4). The curves shown in Fig. 4 suggest that the test specimens exhibit competitive contributions to MR(B,T): in magnetic fields with the induction $B < 6$ T the NMR contribution dominates whereas at $B > 6$ T the PMR contribution becomes predominant, which is in agreement with literary data [23, 38, 36]. As can be seen from the insets in Fig. 4, the maximum absolute value of the NMR effect in Specimen 2 (MR_c) is almost 3 times higher than MR_a. One can furthermore note the following. The NMR effect region in Fig. 4 coincides with the saturation region in the temperature functions of conductivity $\sigma(T)$ at low temperatures (see inset in Fig. 3 *a*). The maximum absolute values of negative $MR_a(B,T)$ for Specimen 1 and the magnetic induction B_m up to which NMR occurs (see curves in the inset of Fig. 4 *a*) are almost insensitive to temperature at $2 < T \leq 10$ K but decline rapidly in the $10 < T \leq 50$ K range. For Specimen 2, $MR_c(B,T)$ in the NMR region declines monotonically with an increase in temperature at $T \leq 25$ K although the position of B_m is almost temperature-insensitive. Possible origins of the NMR effect and its behavior as a function of temperature and magnetic field as well as correlations between $MR(B,T)$ and $\sigma(T)$ for the test specimens will be discussed below.

Analysis of the curves showed that in magnetic fields with magnitudes greater than B_m the absolute values of NMR effect and in the whole range of PMR contribution, the $MR(B)$ curves are proportional to B^2 suggesting its Lorentz nature. One should note a number of specific features inherent to the behavior of this contribution with a change in temperature. At 10 K the magnetoresistive effect (even after subtraction of the NMR contribution) is the smallest (almost zero) as compared with its values at higher temperatures although there are indications [37, 43] that the Lorentz contribution to $MR(B)$ usually decreases, not grows, with an increase in temperature. Furthermore it is at $T = 10$ K that the anisotropy of magnetoresistance is completely eliminated since the $MR(B)$ curves for Specimens 1 and 2 look absolutely identical (see Curves *3* in Fig. 4 *a* and *b*).

As shown above the experiments revealed a strong anisotropy of the electrical conductivity and magnetoresistance, including a change in the sign of the anisotropy coefficient $\alpha = [\sigma_a(T) - \sigma_c(T)]/\sigma_c(T)$. This anisotropy shows itself not only as the dependence of the conductivity and MR on current vector orientation relative to the crystallographic axes of b-P single crystals but also as a change in the course of the $\sigma(T)$ (semiconducting- or metallic-like) curves and the magnetoresistive effect as a function of magnetic field and temperature $MR(B,T)$ (NMR or PMR). As follows from the brief literature review presented above the main features of the $\sigma(T)$, $R_h(B,T)$ and $MR(B,T)$ curves for b-P bulk crystals are explained in different sources within four most widely used approaches.

1. Movement of one type of carriers (holes) in intrinsic b-P crystals (single-band model) [24, 41, 42].

2. Movement of two different-sign carriers with different effective masses in two bands [2, 22, 24, 35, 39, 41] (two-band model).

3. Movement of carriers in large-scale potential pattern relief causing the so-called mobility fluctuations [35, 46, 47].

4. Movement of carriers under strong localization conditions (hopping conductivity of carriers or polarons) [26, 38].

We will now justify the criteria of choosing one of the above listed approaches that we will use hereinafter for analyzing the experimental $\sigma(T)$, $R_h(B,T)$ and $MR(B,T)$ dependences and discussing the measurement results.

The use of the single-band model in the former case for analysis of the movement of one type carriers is most likely incorrect for the following reasons. First, this model is only applicable to undoped b-P which is an intrinsic semiconductor and should have predominantly hole conductivity type since the effective mass of holes is lower than that of electrons [48]. Our Hall effect and thermo-emf measurements suggest the electron conductivity type of the material which testifies either to the presence of donor centers (impurities and/or defects) in the test specimens or to a smaller effective mass of electrons in comparison with that of holes. Secondly, as noted above the single-band model overestimates electron concentration in comparison with literary available data for b-P crystals having the electron conductivity type at high temperatures (see inset in Fig. 3 *b*). Thirdly, as can be seen from the inset in Fig. 5 *a* the behavior of the Hall mobility *vs* temperature dependences $\mu_h(T) = \sigma(T)R_h(T)$ does not agree with any of the known electron scattering mechanisms in semiconductors at high (phonon scattering) and low (scattering at charged impurity ions and defects) temperatures. It should be borne in mind that according to earlier data [49] the Hall mobility *vs* temperature dependences for a homogeneous semiconductor should have an exponential shape $\mu_h(T) \sim T^k$ where the exponent k (curve slope in the $Lg(\mu_h) - Lg(T)$ coordinates, see insets in Fig. 5 *a*) depends on the scattering mechanism and should typically be close to one of the following values: +1, +3/2, –1 or –3/2.

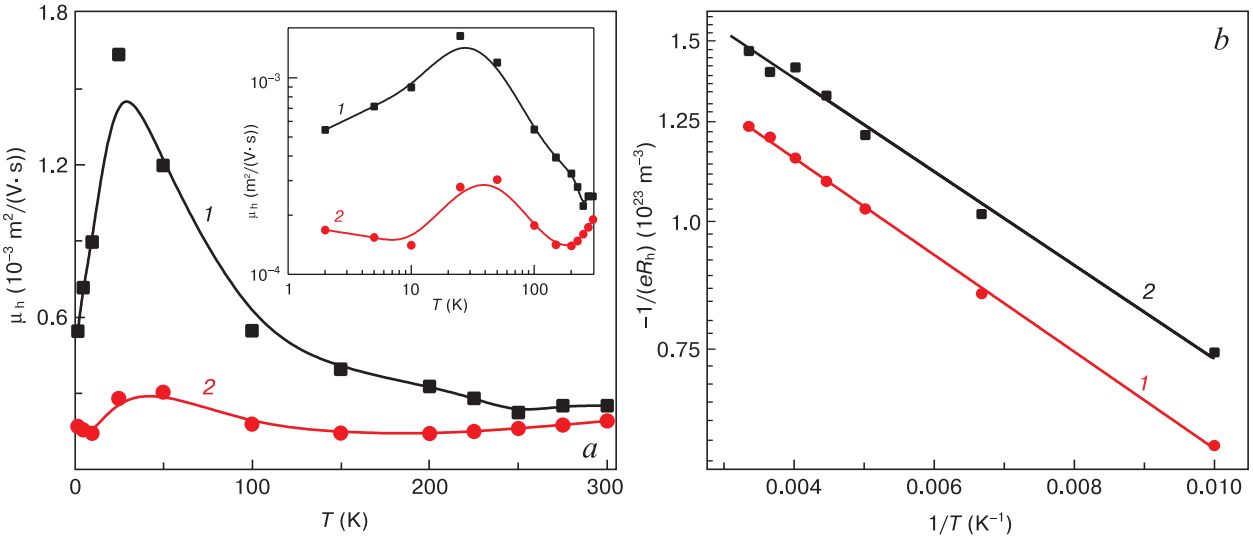

Figure 5. (*a*) Hall mobility *vs* temperature dependences $\mu_h(T)$ in linear coordinates and (*b*) Hall concentration *vs* temperature dependences $n_o(T)$ in double logarithmic coordinates for Specimens (*1*) 1 and (*2*) 2. Inset: $\mu_h(T)$ dependences in double logarithmic coordinates.

The model allowing for carrier movement in the large-scale potential relief region is typically used for analysis of Hall mobility in heavily inhomogeneous semiconductors containing large-scaled structural defects. In b-P crystals these defects can be grain boundaries (in polycrystals), dislocations, interlayer cracks (caused by the extremely high brittleness of these crystals), stacking faults (violation of the layering rule of phosphorus atoms) as well as point defect clusters. The presence of large-scale potential relief in inhomogeneous semiconductor crystals shows itself at low temperatures when and if the temperature dependence of $\mu_h(T)$ in double logarithmic coordinates is linear and has extra large positive slopes (the exponent values $k >> 3/2$) [49]. As can be seen from the inset in Fig. 5 *a*, the $Lg(\mu_h) - Lg(T)$ curves for the test b-P crystals do not exhibit large slopes at low temperatures. Another contribution of large-scale potential relief in inhomogeneous semiconductors [49] should be a transition to a linear magnetoresistance *vs* magnetic field dependence in the PMR region with a decrease in temperature. This $MR(B) \sim B$ dependence for b-P crystals was described earlier in [35] but the $MR(B)$ curves shown above (Fig. 4) do not feature any signs of linear magnetoresistive effect either.

Attempts to describe carrier movement under strong localization conditions showing itself as hopping or polaron conductivity at temperatures below 40–50 K also failed because low-temperature $\sigma(T)$ curves in Mott's coordinates [50] were not linearized.

Analysis of the possibility to use the four abovementioned most widely used approaches to the description of the $\sigma(T)$, $R_h(B,T)$ and $MR(B,T)$ dependences showed that correct description of the magnetoresistive properties of b-P requires the two-band model be used. Note also that when discussing the properties of b-P single crystals we ruled out Drude's theory of quantum corrections to the conductivity due to a carriers phase breaking under weak localization conditions which was formerly observed only in single- or multilayered specimens of splitted phosphorene, graphene and transition metal chalcogenides [38, 44, 45, 47].

For a quantitative evaluation of the parameters describing the conductivity and galvanomagnetic properties of b-P single crystal Specimens 1 and 2 on the basis of the two-band model [51, 53] we will hereinafter use the following relations:

$$\sigma_{xx} = \sum_i \frac{en_i\mu_i}{1+\mu_i^2B^2}; \tag{1a}$$

$$\sigma_{xy} = \sum_i \frac{en_i\mu_i^2B}{1+\mu_i^2B^2}; \tag{1b}$$

$$R_h = r_h \frac{p\mu_p^2 - n\mu_n^2}{e\left(p\mu_p + n\mu_n\right)^2}. \tag{1c}$$

where μ_i, n_i are the mobility and concentration of i-th type carriers ($i = p, n$), respectively, B is the magnetic field induction in which the specimen is located, e is the electron charge and r_h is the Hall factor. Since the Hall coefficient does not depend on magnetic field at $B > 1$ T then assuming electron and hole mobilities to be equal ($\mu_i = \mu$) we can rewrite Eqs. (1a)–(1c) as follows:

$$\sigma_{xx} = \sum_i \frac{en_i\mu_i}{1+\mu_i^2B^2} = \sum_i \frac{en_i\mu}{1+\mu^2B^2} =$$

$$= \frac{e\mu}{1+\mu^2B^2}\sum_i n_i, \tag{2}$$

where

$$n = \sum_i n_i, \tag{3}$$

is the sum of the carrier concentrations. Then Eq. (1a) reduces to the following relation:

$$\sigma_{xx} = \frac{e\mu n}{1+\mu^2 B^2}. \tag{4}$$

Introducing the relationship

$$\rho_{xx} = \frac{1}{\sigma_{xx}} = \frac{1+\mu^2 B^2}{ne\mu} = \frac{1}{ne}\left(\frac{1}{\mu}+\frac{\mu^2 B^2}{\mu}\right) = \\ = \frac{1}{ne}\left(\frac{1}{\mu}+\mu B^2\right). \tag{5}$$

we obtain the formula for relative magnetoresistance tensor:

$$MR_{xx} = \frac{\rho_{xx}(B)-\rho_{xx}(B=0T)}{\rho_{xx}(B=0T)} = \\ = \frac{\left[\left(\frac{1}{\mu}+\mu B^2\right)-\left(\frac{1}{\mu}+\mu 0^2\right)\right]}{\left(\frac{1}{\mu}+\mu 0^2\right)} = \\ = \frac{\left[\left(\frac{1}{\mu}+\mu B^2\right)-\left(\frac{1}{\mu}\right)\right]}{\left(\frac{1}{\mu}\right)} = \frac{\mu B^2}{\frac{1}{\mu}} = \mu^2 B^2, \tag{6}$$

where μ_0 is the mobility at $B = 0$. This implies the equality

$$\mu = \frac{\sqrt{MR_{xx}}}{B}. \tag{7}$$

For the two carrier types having different signs (electrons and holes) and mobilities in classically weak magnetic fields $\mu^2 B^2 << 1$ for which r_h depends on the scattering mechanism [51], it follows from Eq. (1a) that the Hall coefficient can be expressed as follows:

$$R_h = r_h \frac{p\mu_p^2 - n\mu_n^2}{e\left(p\mu_p + n\mu_n\right)^2}, \tag{8}$$

whereas for $\mu_p = \mu_e = \mu$ it transforms as follows:

$$R_h = r_h \frac{(p-n)}{e(p+n)^2}. \tag{9}$$

Therefore, the experimental value $1/eR_h$ will be related to the actual carrier concentrations (n and p) through the following formula:

$$\frac{1}{en_1} = \frac{r_h(p-n)}{e(p+n)^2}; \quad n_1 = r_h\frac{(p+n)^2}{(p-n)}. \tag{10}$$

In this case the conductivities for equal electron and hole mobilities ($\mu_p = \mu_e = \mu$) and for co-existence of two different-sign carrier types will be as follows:

$$\sigma = \sigma_h + \sigma_e = en\mu + ep\mu = e\mu(n+p) = e\mu n_2, \tag{11a}$$

$$\sigma = \sigma_h + \sigma_e = en\mu_e + ep\mu_h, \tag{11b}$$

whence

$$n_2 = (n+p). \tag{12}$$

Therefore, the n_1 parameter in Eq. (10) can be obtained by measuring the Hall coefficient ($1/eR_h$), the n_2 parameter can be borrowed from the conductivity formula (Eq. (11a)) and the mobility can be calculated using Eq. (6) for the MR_{xx} parameter:

$$n_2 = \frac{\sigma}{e\mu} = \frac{\sigma}{e\frac{\sqrt{MR_{xx}}}{B}} = \frac{\sigma B}{e\sqrt{MR_{xx}}}. \tag{13}$$

Simple transformations of Eqs. (1) and (12) yield the following set of equations for n and p calculation:

$$\begin{cases} n = (n_2 - p); \\ p = \dfrac{n_2^2 + n_2 n_1}{2n_1}. \end{cases} \tag{14}$$

The relationships obtained above (Method 1) will be hereinafter used for the calculations of carrier concentrations and mobilities (provided the latter are equal).

To estimate these parameters in the assumption of the electrical neutrality condition (if the b-P crystals are accepted to be intrinsic semiconductors) we will consider the electron and hole concentrations to be equal:

$$n = p. \tag{15}$$

Then the conductivity, the Hall constant and the magnetoresistance will be respectively described by the following relationships [51, 53]:

$$\sigma = \sigma_h + \sigma_e = en\mu_e + ep\mu_h = eN(\mu_e + \mu_h); \tag{16a}$$

$$R_h = r_h \frac{p\mu_h^2 - n\mu_e^2}{e\left(p\mu_h + n\mu_e\right)^2} = r_h \frac{N\mu_h^2 - N\mu_e^2}{e\left(N\mu_h + N\mu_e\right)^2} = \\ = \frac{r_h}{eN}\frac{(\mu_h - \mu_e)}{(\mu_h + \mu_e)} = r_h \frac{(\mu_h - \mu_e)}{\sigma}, \tag{16b}$$

$$MR = \frac{\rho(B)-\rho(0)}{\rho(0)} = \mu_h \mu_e B^2. \tag{16c}$$

Introducing the notations

$$\mu_h - \mu_e = \frac{\sigma R_h}{r_h}; \tag{17a}$$

$$\frac{\sigma R_h}{r_h} = C; \tag{17b}$$

$$\frac{MR}{B^2} = A. \tag{17c}$$

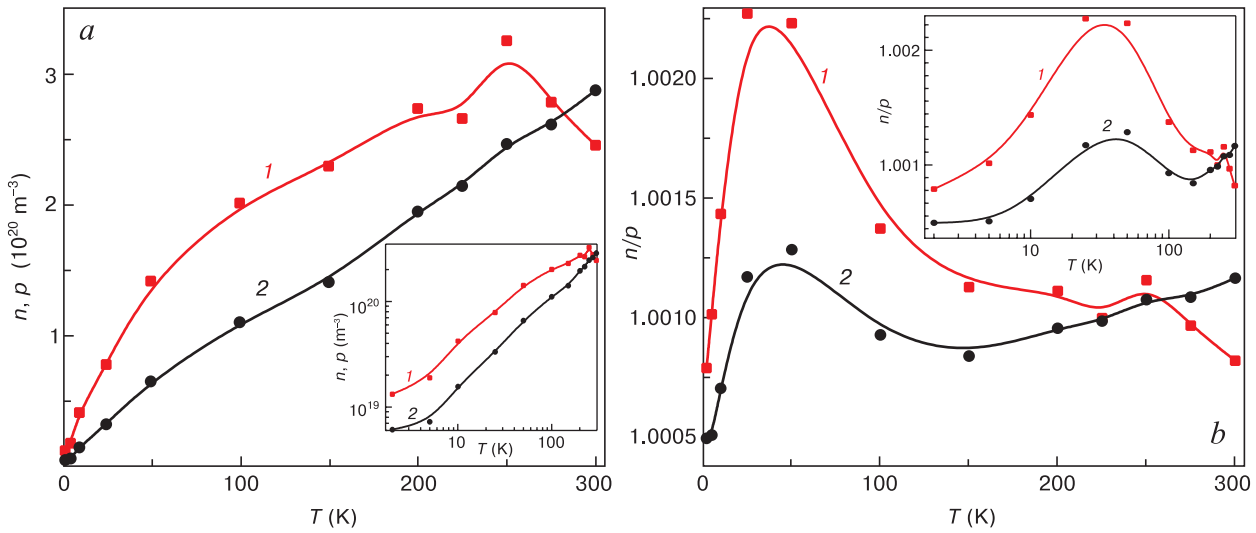

Figure 6. (*a*) Electron and hole concentrations ($n = p$) *vs* temperature and (*b*) electron-to-hole concentration ratio (n/p) for Specimens (*1*) 1 and (*2*) 2. Inset: same functions in double logarithmic coordinates.

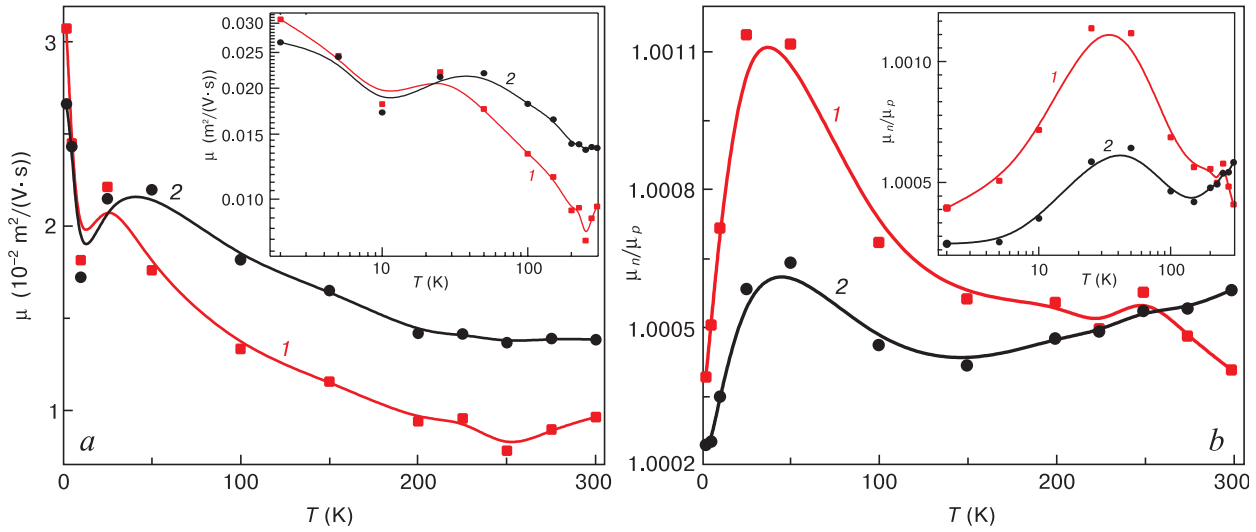

Figure 7. (*a*) Electron and hole mobilities μ(*T*) *vs* temperature and (*b*) electron-to-hole mobility ratio (μ_n/μ_p) for Specimens (*1*) 1 and (*2*) 2. Inset: mobility *vs* temperature in double logarithmic coordinates.

we obtain the following set of equations for the calculation of mobilities:

$$\begin{cases} \mu_h = \dfrac{A}{\mu_e}; \\ \mu_e^2 + C\mu_e - A = 0; \end{cases}$$

$$D = C^2 - 4A,$$

which has two solutions:

$$\begin{cases} \mu_{e1} = \dfrac{-C + \sqrt{D}}{2}; \\ \mu_{e2} = \dfrac{-C - \sqrt{D}}{2}. \end{cases} \qquad (18)$$

Calculations using Eqs. (15)–(18) are the principle of Method 2.

We will now estimate some parameters of the test b-P single crystal specimens using Methods 1 and 2 for the fitting of the galvanomagnetic properties as described above. It should be noted that for calculations based on either of the Methods using the experimentally observed magnetoresistive effect $MR(T,B)$ at temperatures below 25 K we took into account the NMR contribution to the magnetoresistive effect in the region of a magnetic field by subtracting its maximum absolute value at $B = B_m$ (see insets in Fig. 4). The possibility of this allowance for NMR (at least partial) is provided by the fact that the quadratic magnetoresistance vs B dependence exists not only in the PMR region: it starts almost immediately at $B > B_m$ when the NMR contribution is still present. The latter fact suggests that the NMR contribution at above B_m decreases with an increase in B.

Results of fitting using both Methods described above for derivation of the electron and hole concentration and

Table 1. Calculated carrier concentrations and mobilities for $T = 25$ K

Specimen	Concentration (10^{19} m^{-3})			Mobility (m^2/(V·s))		
	n	p	$n = p$	μ_n	μ_p	$\mu_p = \mu_n = \mu$
	Method 1		*Method 2*	*Method 2*		*Method 1*
1	7.878	7.860	7.869	0.02212	0.02210	0.02211
2	3.328	3.332	3.330	0.02148	0.02147	0.02147

mobility temperature dependences yield close values, see Figs. 6 and 7. We further illustrate the proximity of these values by summarizing the calculated p, μ_n and μ_p values for $T = 25$ K in Table 1.

Before discussing the dependences shown in Figs. 6 and 7 one should note that the difference between the electron and hole concentrations calculated using Method 1 in Table 1 is within 0.23% and the results of calculation using Method 2 are intermediate between the respective estimates obtained using Method 1. In order to avoid plotting all the curves calculated by both the methods for all the temperature points (due to their proximity) while analyzing the $n(T)$, $p(T)$, $\mu_n(T)$ and $\mu_p(T)$ dependences, we show only one curve for each specimen in Figs. 6 and 7.

Analysis of the dependences shown in Fig. 6 *a* showed that the electron and hole concentrations ($n = p$) for Specimens 1 and 2 as calculated using Method 1 or Method 2 are by approx. four orders of magnitude lower than the single-band model estimates (Fig. 6 *b* and Fig. 3 *b*). This agrees with earlier data [2, 22, 24]. The data summarized in Table 1 suggest that n and p of both specimens are close and are indeed irresolvable in a typical scale (Fig. 6 *a*). It should be noted that the $n(T)$ and $p(T)$ curves shown in Fig. 6 *a* for Specimen 1 are always above (at least at $T < 250$ K) those for Specimen 2. Furthermore, as can be seen from the insets in Fig. 6 *a* the patterns of the $n(T)$ and $p(T)$ dependences are nearly exponential.

The behavior of the $n(T)$ and $p(T)$ dependences described above suggests that the experimental b-P single crystals are intrinsic semiconductors with predominantly electron conductivity type.

As can be seen from Fig. 7 *a*, the temperature dependences of the carrier mobilities for both carrier signs in both specimens exhibit a nonmonotonic behavior below 25–50 K. Above 25–50 K the carrier mobilities decline with an increase in temperature and as can be seen from the inset in Fig. 7 *a* their curves obey a law close to $\mu(T) \sim T^{-1}$. This $\mu(T)$ behavior was observed earlier [21, 22, 24] and indicates predominant carrier scattering at lattice vibrations. The nonmonotonic behavior of the carrier mobility at low temperatures most probably testifies to insufficient allowance for the effect of the NMR on the PMR at low temperatures which is an indispensable condition for the correct use of Eqs. (1)–(18) for curve fitting. The mobility of the carriers drifting along the *c* axis in most part of the temperature range studied (at $T > 50$ K) is higher than that of the carriers drifting along the *a* axis which is in agreement with earlier data [2, 3].

There is an obvious correlation between the curve behavior shown in Fig. 3 and those in Figs. 6 and 7. This correlation determines the specific features of the conductivity anisotropy that changes its sign at about 225 K. It can be seen from Fig. 6 that the carrier concentration $n(T)$ in Specimen 1 grows with an increase in temperature and sees a saturation plateau at above 200 K. In the meantime, the $\mu(T)$ curve in Fig. 7 *a* on the contrary declines with an increase in T and also tends to saturation above 200 K. As a result, this joint behavior of the $n(T)$ and $\mu(T)$ dependences for Specimen 1 determines the weak $\sigma_a(T)$ dependence above 70 K (Fig. 3 *a*).

On the other hand, since the carrier concentration for Specimen 1 shown in Fig. 6 *a* increases with temperature faster than that for Specimen 2, the $\sigma_a(T)$ curve for Specimen 1 in Fig. 3 *a* is above the $\sigma_c(T)$ curve for Specimen 2. Since the carrier mobility in Specimen 2 grows at above 150 K instead of dropping as for Specimen 1, the $\sigma_c(T)$ curve in Fig. 3 *a* grows instead of seeing a saturation plateau by analogy with the $\sigma_a(T)$ curve for Specimen 1.

It follows from the above that the conductivity anisotropy is mainly determined by the carrier concentration anisotropy. Since the carrier concentration and mobility in Specimen 1 see a saturation plateau at high temperatures whereas the carrier concentration in Specimen 2 always grows with temperature, the sign of the conductivity anisotropy in Specimen 2 changes. Thus the correlation between the temperature behavior of the conductivity shown in Fig. 3 and the electron and hole concentrations and mobilities shown in Figs. 6 and 7 indicates the correctness of the two-band model approach for analysis of carrier transport in the test b-P single crystals.

We will now compare the presence and behavior of the NMR effect in the test b-P specimens at low temperatures (Fig. 4) with the results of the above analysis of the $\sigma_a(T)$, $\sigma_c(T)$, $n(T)$ and $\mu(T)$ temperature dependences. The NMR effect is usually discussed within models describing electron drift under strong and/or weak atomic disorder conditions in crystals when the Lorentz mechanism whereby magnetic field affects carrier movement is no longer active. For relatively weak disorder (weak localization regime) the interaction of electrons with defects and phonons at low temperatures is elastic or quasielastic. Then the carrier drift is described by theory of quantum corrections to the Drude conductivity [44, 54] which postulates that crystals with weak localization may exhibit

the implementation of the so-called self-crossing electron trajectories. Then two clockwise and counterclockwise drifting electrons remain coherent in spite of the scattering because their wavefunction phase does not change. These electrons interfere with each other leading to a lower conductivity as compared with the value suggested by standard quantum theory for Drude conductivity [43, 52]. In accordance with the quantum corrections model [44, 54], application of even a relatively weak magnetic field (typically within $B = 100$ mT) causes phase breaking for these two electrons, i.e., violation of their coherency resulting in the interference of their wavefunctions and hence an increase in the conductivity (i.e., suppression of the quantum corrections). As compared with the Lorentz mechanism of electrical resistivity growth in a magnetic field [43] this behavior is anomalous since it corresponds to the negative magnetoresistive effect. However the NMR effect in the test b-P crystals is observed up to $B \sim 6$ T magnetic fields (Fig. 4) which precludes its description within the quantum corrections theory.

The NMR effect is often observed in strongly disordered semiconductors (i.e., under strong localization conditions) when hopping electron transport over localized states occurs [50]. In this case the $\sigma(T)$ dependence is usually described by the relationship , where T_0 and σ_0 are parameters depending on the density of localized states and the carrier wavefunction localization radius and the exponent is $\eta = 0.25$ for Mott's model and $\eta = 0.5$ for the Shklovsky–Efros theory. The magnetic field dependences of the resistivity $\rho(B)$ in the NMR effect region are described on the basis of the model [55] which implies a relation of the following type: $\rho(B) = -\rho(0)\exp(\gamma/B^m)$. Then the exponential constant γ depends on the type of doping (defectiveness) of the material and the carrier wavefunction localization radius. The use of appropriate fitting procedures for the experimental $\sigma(T)$ and $MR(B)$ dependences unfortunately failed to provide physically justified parameters of the models [50, 55]. Nevertheless some features in the behavior of the $\sigma(T)$ and $MR(B)$ dependences indicate a significant contribution of disorder in the b-P crystals to the variation of the material's conductivity due to temperature and magnetic field. These features are primarily the saturation of the conductivity curve at $T \to 0$ (see inset in Fig. 3 *b*) and the NMR effect itself. It should be therefore borne in mind that in order to successfully describe the experimental $\sigma(T,B)$ dependences on the basis of the quantum corrections [44, 54, 55], hopping conductivity [50, 55] and Schick's models for large-scale potential relef [49] these models should take into account the co-existence of two carrier types and the effect of structural defects induced during the b-P growth stage, specimen transportation and measurement preparation. Possibly, the common disregard to these contributions explains the great variety of literary reported models and approaches to the description of the electrical properties of b-P crystals and the large scatter of experimental results obtained by different experimentalists.

4. Conclusion

Study of the galvanomagnetic properties of black phosphorus (n-P) single crystals showed that these crystals are intrinsic semiconductors with two carrier types (electrons and holes) having almost equal concentrations and mobilities. The temperature dependence of the electrical conductivity $\sigma(T)$ is determined by the orientation of the current vector relative to the *a* and *c* crystallographic axes and depends primarily on the carrier concentration anisotropy. At below 50–70 K the anisotropy coefficient $\alpha = [\sigma_a(T) - \sigma_c(T)]/\sigma_c(T)$ is positive whereas at above 220 K its sign changes to negative. We showed that the resistivity *vs* magnetic field dependences for both specimens incorporate two competing contributions, i.e., the negative (NMR) and positive (PMR). The NMR contribution seems to originate from structural disorder and is observed at $T < 25$ K and $B < 6$ T while the PMR one is associated with the Lorentz mechanism and shows itself at above 25 K in 6–8 T magnetic fields.

References

1. Inamuddin, Boddula R., Asiri A.M. (Eds.). Black phosphorus: synthesis, properties and applications. Springer, 2020, 191 p. https://doi.org/10.1007/978-3-030-29555-4
2. Narita S., Akahama Y., Tsukyama Y., Muro K., Mori Sh., Endo S., Tanlguchi M., Seki M., Suga S., Mikuni A., Kanzaki H. Electrical and optical properties of black phosphorus single crystals. *Physica B. Condensed Matter*, 1983; (117–118): 422–424. https://doi.org/10.1016/0378-4363(83)90547-8
3. Akahama Y., Miyakawa M., Taniguchi T., Sano-Furukawa A., Machida Sh., Hattori T. Structure refinement of black phosphorus under high pressure. *J. Chem. Phys*., 2020; 153(1): 014704. https://doi.org/10.1063/5.0012870
4. Tran V., Soklaski R., Liang Y., Yang L. Layer-controlled band gap and anisotropic excitons in few-layer black phosphorus. *Phys. Rev. B*, 2014; 89(23): 817–824. https://doi.org/10.1103/physrevb.89.235319
5. Brown A., Rundqvist S. Refinement of the crystal structure of black phosphorus. *Acta Cryst*., 1965; 19: 684. https://doi.org/10.1107/S0365110X65004140
6. Baba M., Izumida F., Takeda Y., Shibata K., Morita A., Koike Y., Fukase T. Two-dimensional Anderson localization in black phosphoruscrystals prepared by bismuth-flux method. *J. Phys. Soc. Jpn.*, 1991; 60(11): 3777–3783. https://doi.org/10.1143/JPSJ.60.3777

7. Li C., Tian Z. Thermal transport properties of black phosphorus: a topical review. *Nanoscale Microscale Thermophys*, 2017; 21(1): 45–57. https://doi.org/10.1080/15567265.2016.1278413
8. Wan B., Guo S., Sun J., Zhang Y., Wang Y., Pan C., Zhang. J. Investigating the interlayer electron transport and its influence on the whole electric properties of black phosphorus. *Sci. Bull.*, 2019; 64: 254–260. https://doi.org/10.1016/j.scib.2018.11.026
9. Hirose K., Osada T., Uchida K., Taen T., Watanabe K., Taniguchi T., Akahama Y. Double carrier transport in electron-doped region in black phosphorus FET. *Appl. Phys. Lett.*, 2018; 113(19): 193101. https://doi.org/10.1063/1.5048233
10. Chen X., Ponraj J.S., Fan D., Zhang H. An overview of the optical properties and applications of black phosphorus. *Nanoscale*, 2020; 12(6): 3513–3534. https://doi.org/10.1039/c9nr09122j
11. Bridgman P.W. Two new modifications of phosphorus. *J. Am. Chem. Soc.*, 1914; 36(7): 1344–1363. https://doi.org/10.1021/ja02184a002
12. Gui R., Jin H., Wang Z., Li J. Black phosphorus quantum dots: synthesis, properties, functionalized modification and applications. *Chem. Soc. Rev.*, 2018; 47(17): 6795–6823. https://doi.org/10.1039/c8cs00387d
13. Xia E, Wang H., Jia Y. Rediscovering black phosphorus as an anisotropic layered material for optoelectronics and electronics. *Nat. Commun.*, 2014; 5(1): 4458. https://doi.org/10.1038/ncomms5458
14. Dhanabalan S.C., Ponraj J.S., Guo Z., Li S., Bao Q., Zhang H. Emerging trends in phosphorene fabrication towards next generation devices. *Adv. Sci.*, 2017; 4(16): 1600305. https://doi.org/10.1002/advs.201600305
15. Fu Y., Wei Q., Zhang G., Sun S. Advanced phosphorus-based materials for lithium/sodium-ion batteries: recent developments and future perspectives *Adv. Energy Mater.*, 2018; 8(13): 1702849–1702867. https://doi.org/10.1002/aenm.201702849
16. Chen P., Li N., Chen X., Ong W.J., Zhao X. The rising star of 2D black phosphorus beyond graphene: synthesis, properties and electronic applications. *2D Mater.*, 2017; 5(1): 014002. https://doi.org/10.1088/2053-1583/aa8d37
17. Khandelwal A., Mani K., Karigerasi M.H., Lahiri I. Phosphorene – the two-dimensional black phosphorous: properties, synthesis and applications. *Mater. Sci. Eng. B*, 2017; 221: 17–34. https://doi.org/10.1016/j.mseb.2017.03.011
18. Pumera M. Phosphorene and black phosphorus for sensing and biosensing. *Trends Anal. Chem.*, 2017; 93: 1–6. https://doi.org/10.1016/j.trac.2017.05.002
19. Lei W., Liu G., Zhang J., Liu M. Black phosphorus nanostructures: recent advances in hybridization, doping and functionalization. *Chem. Soc. Rev.*, 2017; 46(12): 3492–3509. https://doi.org/10.1039/c7cs00021a
20. Zhang Y., Wang J., Liu Q., Gu Sh., Sun Zh., Chu P.K., Yu X. The electrical, thermal, and thermoelectric properties of black phosphorus. *APL Materials*, 2020; 8(12): 120903. https://doi.org/10.1063/5.0027244
21. Keyes R.W. The electrical properties of black phosphorus. *Phys. Rev.*, 1953; 92: 580–584. https://doi.org/10.1103/physrev.92.580
22. Warschauer D. Electrical and optical properties of crystalline black phosphorus. *J. Appl. Phys.*, 1963; 34(7): 1853–1860. https://doi.org/10.1063/1.1729699
23. Maruyama Y., Suzuki S., Kobayashi K., Tanuma S. Synthesis and some properties of black phosphorus single crystals. *Physica B+C*, 1981; 105(1–3): 99–102. https://doi.org/10.1016/0378-4363(81)90223-0
24. Akahama Y., Endo S., Narita S. Electrical properties of black phosphorus single cry. *J. Phys. Soc. Jpn.*, 1983; 52(6): 2148–2155. https://doi.org/10.1143/jpsj.52.2148
25. Asahina H., Shindo K., Morita A. Electronic structure of black phosphorus in self-consistent pseudopotential approach. *J. Phys. Soc. Jpn.*, 1982; 51: 1193–1199. https://doi.org/10.1143/jpsj.51.1193
26. Machida Y., Subedi A., Akiba K., Miyake A., Tokunaga M., Akahama Y., Izawa K., Behnia K. Observation of Poiseuille flow of phonons in black phosphorus. *Sci. Adv.*, 2018; 4(6). https://doi.org/10.1126/sciadv.aat3374
27. Zeng Q., Sun B., Du K., Zhao W., Yu P., Zhu C., Xia J., Chen Y., Cao X., Yan Q., Shen Z., Yu T., Long Y., Koh Y.K., Liu Z. Highly anisotropic thermoelectric properties of black phosphorus crystals. *2D Mater.*, 2019; 6(4): 045009. https://doi.org/10.1088/2053-1583/ab2816
28. Rodrigues E.F.S., Gainza J., Serrano-Sanchez F., Lopez C., Dura O.J., Nemes N., Martinez J.L., Huttel Y., Fauth F., Fernandez-Diaz M.T., Biškup N., Alonso J.A. Structural features, anisotropic thermal expansion, and thermoelectric performance in bulk black phosphorus synthesized under high pressure. *Inorg. Chem.*, 2020; 59(20): 14932–14943. https://doi.org/10.1021/acs.inorgchem.0c01573
29. Fei R.; Yang L. Strain-engineering the anisotropic electrical conductance of few-layer black phosphorus. *Nano Lett.*, 2014; 14(5): 2884–2889. https://doi.org/10.1021/nl500935z
30. Qiao J., Kong X., Hu Z.-X., Yang F., Ji W. High-mobility transport anisotropy and linear dichroism in few-layer black phosphorus. *Nat. Commun.*, 2014; 5(1): 4475. https://doi.org/10.1038/ncomms5475
31. Zeng Q., Sun B., Du K., Zhao W., Yu P., Zhu Ch., Xia J., Chen Y., Cao X., Yan Q., Shen Z., Yu Ti., Long Y, Koh Y.K., Liu Zh. Highly anisotropic thermoelectric properties of black phosphorus crystals. *2D Mater.*, 2019; 6(4): 045009. https://doi.org/10.1088/2053-1583/ab2816
32. Morita A. Semiconducting black phosphorus. *Appl. Phys. A. Solids and Surfaces*, 1986; 39(4): 227–242. https://doi.org/10.1007/bf00617267
33. Shirotani I., Maniwa R., Sato H., Fukizawa A., Sato N., Maruyama Y., Kajiwara T., Inokuchi H., Akimoto S. Preparation, growth of large single-crystals, and physicochemical properties of black phosphorus at high-pressures and temperatures. *Nippon Kagaku Kaishi*, 1981; 10: 1604–1609. (In Jpn.). https://doi.org/10.1246/nikkashi.1981.1604
34. Tao J., Shen W., Wu S., Liu L., Feng Z., Wang C., Hu C., Yao P., Zhang H., Pang W., Duan X., Liu J., Zhou C., Zhang D. Mechanical and electrical anisotropy of few-layer black phosphorus. *ACS Nano*, 2015; 9(11): 11362–11370. https://doi.org/10.1021/acsnano.5b05151
35. Hou Z., Yang B., Wang Y., Ding B., Zhang X., Yao Y., Liu E., Xi X., Wu G., Zeng Z., Liu Z., Wang W. Large and anisotropic linear magnetoresistance in single crystals of black phosphorus arising from mobility fluctuations. *Sci. Rep.*, 2016; 6: 1–7. https://doi.org/10.1038/srep23807
36. Strutz T., Miura L.N., Akahama Y. Magnetotransport investigation on black phosphorus at low Temperatures. *Phys. B. Condensed Matter*, 1994; 394–396(1–2): 1185–1186. https://doi.org/10.1016/0921-4526(94)90922-9

37. Kohler M. Zur magnetischen Widerstandsänderung reiner Metalle. *Annalen der Physik*. 1938; 424(1–2): 211–218. (In Ger.). https://doi.org/10.1002/andp.19384240124
38. Jiang X.H., Xiong F., Zhang X.W., Hua Z.H., Wang Z.H., Yang S.G. Large Magnetoresistance and hall effect in paramagnetic black phosphorus synthesized from red phosphorus. *J. Phys. D: Appl. Phys.*, 2018; 51(9): 195101. https://doi.org/10.1088/1361-6463/aab6fa
39. Akiba K., Miyake A., Akahama Y., Matsubayashi K., Uwatoko Y., Tokunaga M. Two-carrier analyses of the transport properties of black phosphorus under pressure. *Phys. Rev. B*, 2017; 95: 115126. https://doi.org/10.1103/physrevb.95.115126
40. Endo S., Akahama Y., Terada S., Narita S. Growth of large single crystals of black phosphorus under high pressure. *Jpn. J. Appl. Phys.*, 1982; 21(8): L482–L484. https://doi.org/10.1143/jjap.21.l482
41. Keyes R. The electrical properties of black phosphorus. *Phys. Rev.*, 1988; 92: 580–584. https://doi.org/10.1103/physrev.92.580
42. Fedotov A.K., Kharchanka A., Fedotova J., Slabuho V., Bushinski M., Svito I. Electric properties of black phosphorus single crystals. In: *IX Intern. Sc. Conf.: Actual Problems of Solid State Physics*. Minsk: Publisher A.Varaksin, 2021; 2: 47–51. http://apssp2021.site/files/APSSP-2021_Proceedings_Book_21.pdf
43. Pippard A.B. Magnetoresistance in metals. Cambridge; London: Cambridge University Press; 1989. 253 p.
44. Altshuler B.L., Aronov A.G., Khmelnitsky D.E. Effects of electron-electron collisions with small energy transfers on quantum localization. *J. Phys. C: Solid State Phys.*, 1982; 15(36): 7367. https://doi.org/10.1088/0022-3719/15/36/018
45. Du Y., Neal A.T., Zhou H., Peide D.Y. Weak localization in few-layer black phosphorus. *2D Materials*, 2016; 3(2): 024003. https://doi.org/10.1088/2053-1583/3/2/024003
46. Parish M.M., Littlewood P.B. Non-saturating magnetoresistance in heavily disordered semiconductors. *Nature*, 2003; 426(6963): 162–165. https://doi.org/10.1038/nature02073
47. Zhang Y.W., Ning H.L., Li Y.N., Liu Y.Z., Wang J. Negative to positive crossover of the magnetoresistance in layered WS_2. *Appl. Phys. Lett.*, 2016; 108(15): 153114. https://doi.org/10.1063/1.4946859
48. Banerjee S., Pati S.K. Charge-transport anisotropy in black phosphorus: critical dependence on the number of layers. *Physical Chemistry Chemical Physics*, 2016; 18(24): 16345–16352. https://doi.org/10.1039/c6cp02129h
49. Shik A.Y., Electronic properties of inhomogeneous semiconductors. Electrocomponent Science Monographs. CRC Press, 1995. 151 p.
50. Shklovskii B.I., Efros A.L. Electronic properties of doped semiconductors. In: *Springer Series in Solid-State Sciences*. Berlin; Heidelberg: Springer-Verlag, 1984, 400 p. https://doi.org/10.1007/978-3-662-02403-4
51. Kuchis E.V. Methods for studying the Hall effect. Moscow: Radio i svyaz, 1990, 264 p. (In Russ.)
52. Ashcroft N.W., Mermin N.D. Solid state physics. New York: Saunders College Publishing, 1976.
53. Asahina H., Shindo K., Morita A. Electronic structure of black phosphorus in self-consistent pseudopotential approach. *J. Phys Soc. Jpn.*, 1982; 51: 1193–1199. https://doi.org/10.1143/jpsj.51.1193
54. Pudalov V.M. Metallic conduction, apparent metal-insulator transition and related phenomena in two-dimensional electron liquid. In: *Proceedings of the International School of Physics "Enrico Fermi"*. 2004; 157: 335–356.
55. Altshuler B.L., Aronov A.G., Khmelnitsky L.E. Negative magnetoresistance in semiconductors in the hopping conduction region. *JETP Letters*, 1982; 36(5): 157–160. (In Russ.)